

Reconfigurable all-in-one chaotic computing with skyrmions: Leveraging periodic modulations of perpendicular magnetic anisotropy

Gyuyoung Park  and Sang-Koog Kim ^{*}

National Creative Research Initiative Center for Spin Dynamics and Spin-Wave Devices, Nanospinics Laboratory, Research Institute of Advanced Materials, Department of Materials Science and Engineering, Seoul National University, Seoul 08826, Republic of Korea



(Received 5 March 2024; revised 15 April 2024; accepted 16 April 2024; published 9 May 2024)

Magnetic skyrmions became critical elements in spintronics. Our study, through micromagnetic simulations, reveals that skyrmions experience chaotic changes in topological charge when exposed to sinusoidal variations in perpendicular magnetic anisotropy. This work introduces the following concept: a logic device based on a single skyrmion, which we envision as a stepping stone in chaotic computing. This conceptual device is designed to perform various logic operations in a reconfigurable format. We demonstrate the concept's feasibility by implementing sixteen 2-input logic gates, whose functionality depends on the skyrmion's initial conditions. These initial conditions can be manipulated by a current, accompanied by spin-orbit torque and the subsequent skyrmion-Hall effect. Our study presents an optimized logic operation map, highlighting specific initial conditions for corresponding logic operations. This work may provide the concept of a magnetic-field-free, low-power logic device, potentially contributing significantly to the development of advanced spintronic computing paradigms.

DOI: [10.1103/PhysRevB.109.174420](https://doi.org/10.1103/PhysRevB.109.174420)

I. INTRODUCTION

Perpendicular magnetic anisotropy (PMA), which shapes the magnetization direction normal to the surface or interface, has played a crucial role in spintronics thanks to its superior thermal stability, energy efficiency, and scaling properties [1–3]. PMA has been widely manipulated in various systems such as transition metal/oxide interfaces [4], heavy-metal/ferromagnet [5], two-dimensional materials [6], and L_{10} magnetic alloys [7] to control magnetization in soft [8] and hard magnets [9] as well as magnetization switching in magnetic nanoelements in storage devices and spintronics. In particular, the introduction of voltage-controlled magnetic anisotropy (VCMA) has sparked considerable interest due to its ability to manipulate magnetizations without applying magnetic fields or currents [10]. Its significance in spintronics lies in its capacity for low-power-driven magnetization switching [11].

The advent of PMA not only advanced spintronics but also played a pivotal role in the emergence and sophisticated control of nontrivial topological spin textures, particularly magnetic skyrmions [12–14], thereby significantly contributing to the field of skyrmionics [15]. The magnetic skyrmions have garnered focus for their topological stability, leading to potential applicability in low-power-driven high-density data storage and fast information processing devices at the nanoscale [16–18]. Exciting skyrmions not only through electric currents [19,20], spin-transfer torques [18], spin-orbit torques (SOTs) [21], and thermal fluctuation [22] but also via PMA show promise for their applications in

spintronic information processing devices [23–26]. Specifically, skyrmionics has recently expanded to include unconventional computing approaches such as artificial neural networks [27], synaptic devices [28], neuromorphic computing [29,30], Brownian reservoir computing [31], probabilistic computing [32], reshuffle devices [33], and quantum computing [34,35]. Other potential examples are explorations of chaotic dynamics within skyrmions driven by magnetic field [36] and current [37], which can potentially offer an advanced scheme for chaotic computing [38,39]. However, research into the ordered or chaotic dynamics of skyrmions modulated by PMA is still unexplored.

This study explores an advanced computation platform using the chaotic switching dynamics of magnetic skyrmions confined in a nanodisk driven by PMA modulation. Inspired by the concept of “dynamics-based computation” by Sinha *et al.* [38,39], we focus on chaotic logic gates that can switch between different logic operations, like OR and AND logics, based on the initial conditions of the skyrmion. By manipulating PMA modulation, we achieved diverse dynamic patterns, enabling various logic operations according to different initial conditions. This research explores the potential of skyrmion-based chaotic computing, featuring reconfigurable all-in-one logic operations, as an innovative advancement in spintronics.

II. METHODS

In this study, we used a model system consisting of a single skyrmion in a circular nanodisk with a radius of 40 nm [23]. We assumed a CoFeB/MgO interface with PMA. To simulate the time-variable magnetization in the nanodisk, we employed the MUMAX³ code, which implements the Landau-Lifshitz-Gilbert equation: $\partial \mathbf{M} / \partial t =$

^{*}Corresponding author: sangkoog@snu.ac.kr

$-\gamma \mathbf{M} \times \mathbf{H}_{\text{eff}} + (\alpha/M_s) \mathbf{M} \times \partial \mathbf{M} / \partial t$, where \mathbf{M} is the magnetization, γ the gyromagnetic ratio, α the Gilbert damping constant, M_s the saturation magnetization, and \mathbf{H}_{eff} the effective field, calculated as $\mathbf{H}_{\text{eff}} = -(1/\mu_0) \partial E_{\text{tot}} / \partial \mathbf{M}$. The total energy, E_{tot} , includes magnetostatic, magnetocrystalline anisotropy, exchange, and intrinsic Dzyaloshinskii-Moriya interaction (DMI), and Zeeman energies. Notably, no Zeeman field was applied in our system. For the CoFeB/MgO interface, we used the following variables: $\alpha = 0.03$, $M_s = 1$ MA/m, exchange constant $A_{\text{ex}} = 20$ pJ/m, and interfacial DMI constant $D_{\text{int}} = 3$ mJ/m² [40]. The cell size was set to $1 \times 1 \times 1$ nm³.

With the conditions specified above, we introduced a skyrmion of Néel type with a topological charge of -1 (core polarization down) and relaxed into its ground state, achieving a skyrmion radius [41] around 17.5 nm. Subsequently, we modulated PMA sinusoidally along time, as $K_u(t) = K_0(1 + \kappa \sin(2\pi ft))$, where $K_0 = 0.8$ MJ/m³. The frequency of the modulation, denoted as f , ranged from 0.01 to 10 GHz, varying in increments of 0.01 GHz. Concurrently, the parameter κ ($0 < \kappa \leq 1$) was varied in increments of $\frac{1}{800}$ ($= 0.00125$). A value of κ exceeding 1 would result in negative PMA values during the modulation. We also changed the number of periods, n , for the sinusoidal PMA modulation. The same initial ground state of the magnetic skyrmion was used for each simulation with varying parameters of (f, κ, n) .

The skyrmion's inherent topological properties were characterized by its topological charge, Q , defined as $Q = \frac{1}{4\pi} \int \mathbf{m} \cdot (\partial_x \mathbf{m} \times \partial_y \mathbf{m}) dx dy$, where the local magnetization direction can be written in polar coordinate, $\mathbf{m}(\mathbf{r}) = \mathbf{m}(\theta, \phi) = (\sin\theta \cos\phi, \sin\theta \sin\phi, \cos\theta)$. Additionally, the helicity number is $Q_h = \phi - Q_v \varphi$ where the vorticity number $Q_v = \frac{1}{2\pi} \oint_c d\phi$ [42].

III. RESULTS

A. Variations of skyrmion's topological charge through PMA modulation

Figure 1 illustrates the magnetization reversal process of a skyrmion in a nanodisk driven by a single period of the PMA $(f, \kappa) = (0.5 \text{ GHz}, 0.7)$ sinusoidal modulation (see blue line at the top of Fig. 1). The topological charge Q (black) and the helicity Q_h (red), which vary during the PMA modulation, are plotted as functions of time. Snapshot images of spin configurations at specific times, labeled as A, B, C, and D, are shown at the bottom of Fig. 1. The skyrmion transitions from an initial state of $(Q, Q_h) = (-1, 0)$ to $(1, \pi)$ after the given single-period modulation. Consequently, the core polarization at the initial state turns out to be spin up (D state) from spin down (A state). The skyrmion disappears through the B state to the C state ($|Q| < 0.5$). Notably, immediately following state B, spin waves are generated at the disk's center and propagate towards its edges. This phenomenon occurs when the skyrmion is annihilated, a process similarly observed during the magnetic vortex switching, as detailed in Ref. [43] and illustrated in the Supplemental Material video [44]. In more detail, with increasing PMA, the skyrmion's radius [41] decreases, then turns into a magnetic vortexlike state and eventually becomes a ferromagnetic state ($Q \approx 0$)

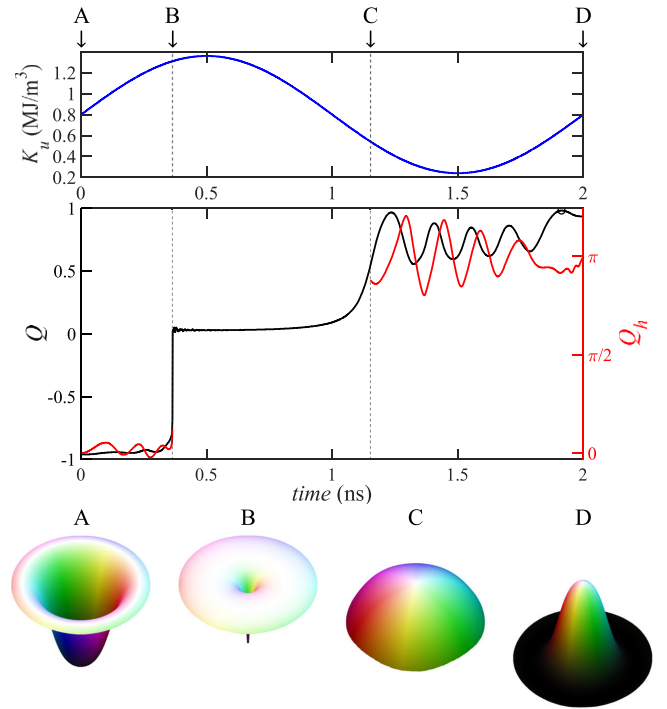


FIG. 1. Variation of topological charge (Q , black line) and helicity (Q_h , red line) of a given skyrmion during the modulation of perpendicular magnetic anisotropy over time (illustrated by the blue line at the top), where $K_u(t) = K_0[1 + \kappa \sin(2\pi ft)]$, $0 < \kappa \leq 1$. Example modulation parameters are $\kappa = 0.7$ and $f = 0.5$ GHz. A black circle indicates a maximum value of the topological charge, Q_{max} , during the modulation. The bottom section shows four distinct spin configurations of the nanodisk, labeled A, B, C, and D at specific times, marked by arrows and dashed lines. The spin direction is depicted using the HSV color scale, and the contour height additionally represents the M_z/M_s component.

with magnetizations aligning along upwards. Noticeably, Q and Q_h fluctuate with a small amplitude between A and B states and with a relatively large amplitude between C and D states.

Figure 2 shows the maximum value of topological charge, Q_{max} , in the nanodisk during the single-period modulation of PMA on the plane of (f, κ) . For example, Q reaches $Q_{\text{max}} \approx 1$ at 1.9 ns (indicated by a black circle), under the condition of $(f, \kappa) = (0.5 \text{ GHz}, 0.7)$, as illustrated in Fig. 1. The phase diagram shown in Fig. 2 is informative regarding the conditions under which the skyrmion transitions to other spin configurations. The red region indicates that the core polarity of the skyrmion was reversed, although this does not guarantee that the Q remains in the $+1$ state after the end of PMA modulation. In some modulation parameters, the Q returns to the -1 state. The yellow region signifies that the skyrmion briefly assumed a half-skyrmion state, while the green region denotes a temporary ferromagnetic state. The blue region indicates that the skyrmion maintains its initial topology during the modulation. As f increases, the threshold PMA at which the skyrmion transitions to the ferromagnetic state decreases linearly [44]. This suggests that the transformation of the skyrmion's spin configuration depends on the rate of variation in PMA.

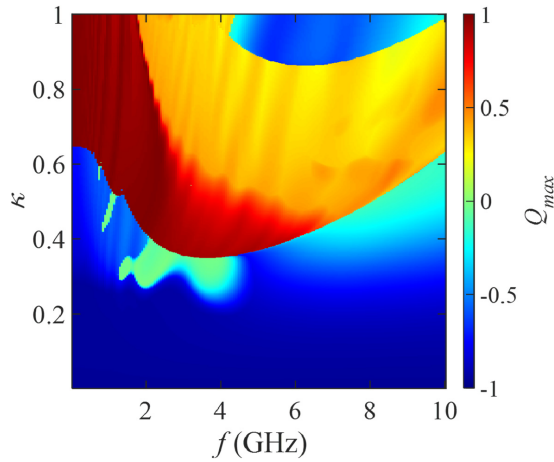


FIG. 2. Phase diagram of maximum topological charge, Q_{\max} , observed in the nanodisk during the sinusoidal modulation of PMA across various (f, κ) values.

Next, the final values of the topological charge just after the n th cycle of the PMA modulations, Q_n , are plotted in Fig. 3, where n represents the number of periods of sinusoidal PMA modulation. As previously mentioned, the spin texture in the red region initially achieved a skyrmion state, indicated by $Q_1 = +1$. However, some reverted to the ferromagnetic state, as indicated by $Q_1 = 0$, with green stripes marking this transition at the top-left part of the figure. In some blue regions, where the Q_{\max} approached 0.5, the spin texture eventually transitioned back to skyrmions, now with $Q_1 = -1$. This indicates that the stability of the transformed state is significantly influenced not only by the threshold K_u value and the rate of K_u variation but also by the spin texture's inherent response to the K_u changes.

In certain regions, ordered patterns become apparent. For instance, one can observe that Q_n is $+1$ (indicated in red) when n is an odd number, and Q_n is -1 (indicated in blue)

when n is an even number, which results in an alternating sequence: $+1, -1, +1, -1$, and so forth. Conversely, certain regions exhibit the opposite behavior: $Q_n = -1$ for even n and $Q_n = +1$ for odd n . To compare this difference, Fig. 3 arranges odd-numbered patterns in the top row and even-numbered patterns in the bottom row. Throughout $n = 1-10$, areas shaded in blue, consistently exhibit a pattern of $Q_n = -1$, indicating simplicity in their behavior. Similarly, the green stripes, as mentioned, consistently represent $Q_n = 0$. A more complex sequence also emerges; for instance, a repeating pattern of $+1, +1, -1, -1$ can be seen near $(f, \kappa) \approx (5 \text{ GHz}, 0.4)$. In areas with higher (f, κ) values, the top-right part of the phase diagram, the patterns become obscured as phases start to mix with increasing n . This blending process seems to plateau at $n = 6$; beyond this cycle, neighboring points display behaviors that are independent of each other, resulting in disordered patterns. Disordered patterns also arise at lower (f, κ) values $\approx (5 \text{ GHz}, 0.25)$. The various patterns are categorized and detailed in the following section.

B. Diverse patterns of Q_n

Figure 4(a) shows eight selected ordered patterns of Q_n ($n = 1-10$). We categorized distinct Q_n patterns with similar trends into groups. In the first pattern, (a1), Q_n alternates between $+1$ and -1 for odd and even n , respectively. The second pattern, (a2) shows Q_n alternating between -1 and $+1$ for odd and even n , respectively. In the third pattern, (a3), Q_n repeats “ $+1, +1, -1, -1$.” In the opposite way, the fourth pattern, (a4), exhibits Q_n repetition of “ $-1, -1, +1, +1$.” In the fifth pattern, (a5), Q_n remains constantly at -1 , while in the sixth pattern, (a6), it stays at 0 . The seventh pattern, (a7), features Q_n alternating between $+1$ for odd n and 0 for even n . The eighth pattern, (a8), shows Q_n switching between 0 at odd n and -1 at even n . In addition to the 8 distinct patterns, 337 additional patterns were observed [44]. These ordered Q_n patterns imply that the magnetization dynamics of the skyrmion are periodic under the sinusoidal

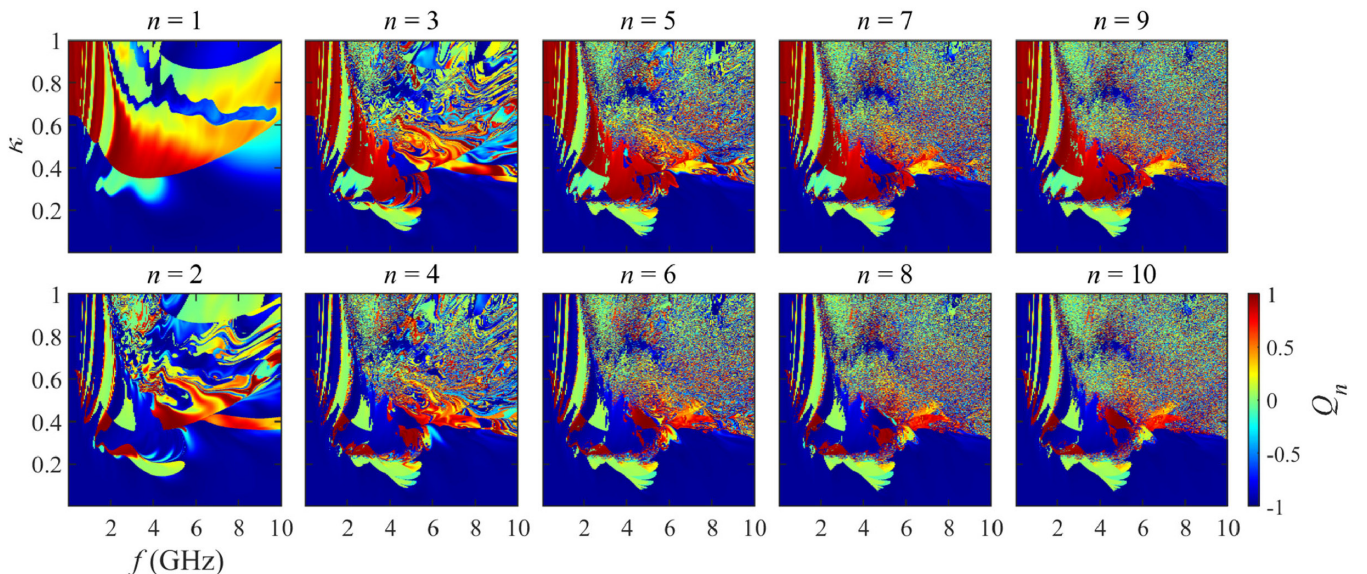


FIG. 3. Nanodisk's topological charge, Q , reached after the indicated n th cycles ($n = 1-10$) of the sinusoidal modulation of PMA across various (f, κ) values.

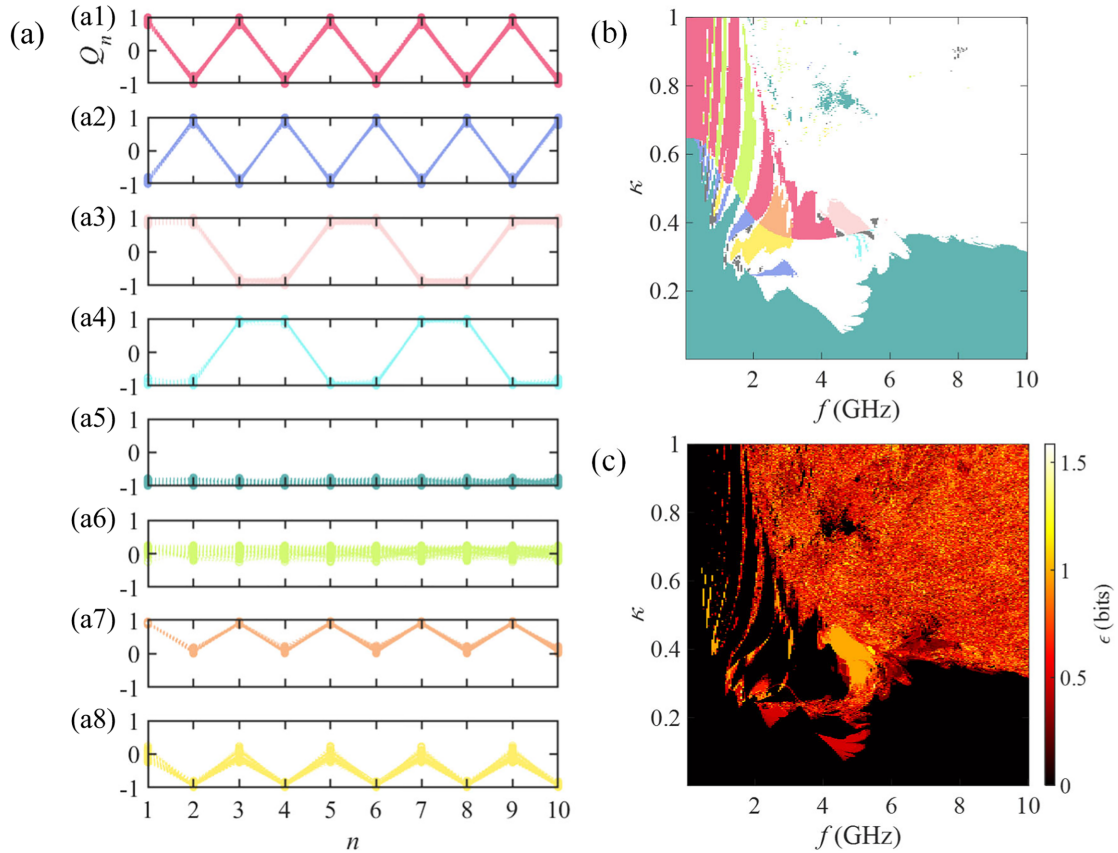


FIG. 4. (a) Various patterns of Q_n during the PMA modulations with $n = 1 - 10$, where different colors indicate distinct patterns, representing different ordered dynamics. (b) Phase diagram of Q_n patterns, where each color corresponds to the dynamic patterns shown in (a). The white regions denote Q_n patterns with lack of order, which are not necessarily chaotic. (c) The entropy of the Markov chain, ϵ , calculated for Q_n . White or yellow regions indicate Q_n with higher information content, while the ordered region is highlighted in black.

modulation of the PMA, offering a method for deterministic control of the skyrmion's topological charge. For instance, a single period ($n = 1$) of the sinusoidal PMA modulation in patterns (a1), (a3), and (a7), deterministically converts the skyrmion from $Q = -1$ to $Q = 1$. Conversely, in patterns (a6) and (a8), a single period of the modulation deterministically annihilates the skyrmion. The PMA modulation in pattern (a5) maintains the skyrmion with $Q = -1$.

In Fig. 4(b), a phase diagram is presented, classifying ordered and disordered patterns, each marked by different colors. These colored regions correspond to the color index for patterns (a1)–(a8). There are eight additional patterns [not shown in Fig. 4(a)] depicted in gray. It is notable that similar patterns, like (a7) and (a8), are located adjacent to each other, across a separating barrier line which is described in Fig. 2. Regions colored with white represent disordered dynamic patterns. Additionally, there may exist other complex yet potentially ordered patterns observable in sequences of Q_n for $n > 10$, in 47498 different patterns that have not been classified in this study. Overall, out of the potential 59049 ($= 3^{10}$) patterns, 47506 distinct patterns arose. This phase diagram suggests that the skyrmion, subject to a given periodic PMA modulation, could serve as a versatile pattern generator for creating ordered and disordered sequences, as mapped out in the phase diagram.

In our study, the sequence of Q_n was conceptualized as a Markov chain, grounded in the hypothesis that its sequential evolution exhibits a memoryless characteristic. This means that each state in the sequence, Q_n , is assumed to be dependent solely on its immediate predecessor, Q_{n-1} , adhering to the Markov property. It is important to note that for a sequence characterized by chaotic dynamics, the correlation between successive states (Q_{n-1} and Q_n) tends to be weaker, leading to increased unpredictability. In chaotic systems, while there might be a deterministic underpinning, the sensitivity to initial conditions and the consequent divergence of trajectories make long-term prediction challenging.

To quantify the complexity inherent in this Markovian sequence, we employed entropy calculation. The entropy of a Markov chain serves as a measure of uncertainty or randomness in the state transitions. A higher entropy value corresponds to greater unpredictability and complexity, indicating a weaker correlation between successive states and, hence, a closer alignment with chaotic behavior. Conversely, lower entropy suggests more predictable and orderly transitions, characteristic of less chaotic sequences. In Fig. 4(c), we display the information entropy of the Markov chain, ϵ , for each Q_n sequence. The values in the Q_n sequence were classified into three states: -1 , 0 , and $+1$. Q_n values ranging from 0.25 to 0.75 and from -0.75 to -0.25 were disregarded.

The maximum value of ϵ , calculated as $\log_2 3$, is 1.585. The calculation methodology is detailed in Appendix A. Notably, nearly all ordered patterns exhibit an entropy value near 0 (black color), indicating minimal randomness. However, certain patterns, such as (a3) and (a4), are with ϵ values around 1, due to their more complex nature. In the white regions of Fig. 4(b), where Q_n is disordered, the entropy is relatively higher. Regions with suspected chaotic Q_n display high values of ϵ . Additionally, patterns characterized by periodic conversion dynamics demonstrate stable energetics, whereas those with suspected chaotic dynamics exhibit instability in their energetics [44].

Furthermore, the Q values of the skyrmion postrelaxation from Q_n , Q_{nr} , show no consistent correlation with the pre-relaxation values of Q_n within the chaotic regions. In periodic regions, Q_{nr} values closely match Q_n . For example, Q_{10r} is close to +1 when Q_{10} is around +1. However, in chaotic regions, Q_{10r} values ranged diversely from -1 to $+1$, even though Q_{10} was approximately 0. Similarly, Q_{10r} could be $+1$, even when Q_{10} was close to -1 . For a detailed examination of how Q_{10} and Q_{10r} correlate across ordered, disordered, and chaotic regimes, see the Supplemental Material [44]. This observation highlights the initial-condition sensitivity in Q_n variations; Q_n varies when the skyrmion's initial conditions are altered, even under identical PMA modulation parameters (f, κ). This phenomenon further supports the existence of chaos in skyrmion dynamics under periodic PMA modulations. Leveraging the chaotic dynamics of skyrmions, it is possible to design computing schemes and devices.

C. Chaotic computation scheme

Utilizing the sensitive dependence on initial conditions, we propose a concept for chaos computation. In this approach, a single skyrmion geometrically confined in nanoelements acts as a chaotic logic gate, forming the basic unit of the chaotic computation scheme. This concept makes a given logic gate reconfigurable since different types of logic operations are possible when its initial condition is varied. Below, the chaos computing scheme is described in three steps.

In step 1, the initial condition of the single skyrmion in the chaotic logic gate is set based on a previously obtained initial-condition map. The skyrmion's initial condition, Q_0 , was manipulated by a charge current density (J ; see Appendix B), determining the specific logic operation to be performed. For example, the current density of J_1 is used for OR logic, while J_2 is set for AND logic. Table I shows all 16 possible truth tables operated by two-input signals (I_1, I_2). It includes six out of seven basic logic operations, excluding the unary NOT operation, and ten additional logic operations. These different logic operations are labeled with integers from 0,1,2, ...,15. The Boolean expressions for these additional logic operations are not exclusive. For example, not only $(A+B)+\bar{A}$, but also $(A+B)+\bar{B}$ lead to the "constant 0" logic operation, as labeled with 0 in Table I. If the desired logic operation is AND, the corresponding initial core position of the skyrmion is set as indicated by the initial-condition map.

In step 2, an input signal is applied to the chaotic logic gate. The PMA of the nanodisk is modulated according to the input signal, causing the topological charge of the nanodisk to

TABLE I. The truth table for the 16 possible two-input logic operations (I_1, I_2) is presented, with the output indicated by O . This set includes six basic logic operations (AND, OR, NAND, NOR, XOR, XNOR) along with ten additional logic operations. Each operation is uniquely assigned a label from 0 to 15.

(I_1, I_2)	(0,0)	(1,0)	(0,1)	(1,1)	Boolean expression	Gate	Label
	0	0	0	0	$(A+B)+\bar{A}$		0
	1	0	0	0	$\bar{A}+\bar{B}$	NOR	1
	0	1	0	0	$\bar{A}\cdot B$		2
	1	1	0	0	$(A\cdot B)+A$		3
	0	0	1	0	$A\cdot\bar{B}$		4
	1	0	1	0	$(A+B)\cdot B$		5
	0	1	1	0	$A\oplus B$	XOR	6
O	1	1	1	0	$\bar{A}\cdot\bar{B}$	NAND	7
	0	0	0	1	$A\cdot B$	AND	8
	1	0	0	1	$A\oplus\bar{B}$	XNOR	9
	0	1	0	1	$(A+B)\cdot B$		10
	1	1	0	1	$\bar{A}+B$		11
	0	0	1	1	$(A\cdot B)+A$		12
	1	0	1	1	$A+\bar{B}$		13
	0	1	1	1	$A+B$	OR	14
	1	1	1	1	$(A+B)+\bar{A}$		15

vary in the chaotic regime. The number of input combinations is 2^m for m -input logics; for example, for two-input signals (I_1, I_2), the four combinations are (0,0), (1,0), (0,1), and (1,1). Therefore, four different PMA modulations are required to emulate the two-input logic operations. In our study, κ values were varied as $\kappa_1, \kappa_2, \kappa_3,$ and κ_4 , while f and n of the PMA modulations were held constant.

In step 3, we estimate the final value of Q_{nr} to determine the output value. If Q_{nr} is $+1$, the output is deemed true; if not, it is considered false. This approach enhances energy efficiency and offers technological benefits, particularly in magnetic tunnel junction (MTJ) configurations. A critical benefit is the ability of tunneling magnetoresistance to accurately detect the Q_{nr} state of the nanodisk, which is considered a significant advantage [45]. Moreover, SOTs enabled all-electrical read-out methods are energetically advantageous [46]. Once the output is assessed, the logic gate is reset to prepare for the subsequent logic operation. Within this framework, the PMA modulations in the ordered regime, specifically through patterns (a1) and (a2), change a skyrmion's Q_{nr} value from $+1$ to -1 . Similarly, a skyrmion with $Q_{nr} = 0$ is converted to -1 through PMA modulations as depicted in pattern (a8).

D. Initial-condition mapping

Building an initial-condition map is an essential part of designing the chaotic logic gate. This map serves as a reference for the chaotic computer to execute specific logic operations. Therefore, it is important to conduct a thorough search for gate conditions, including initial conditions and control parameters, that yield an optimal initial-condition map. This ensures the reliable functioning of the chaotic computer. For instance, drawing inspiration from the ensemble of simulations [47], we suggest constructing the map

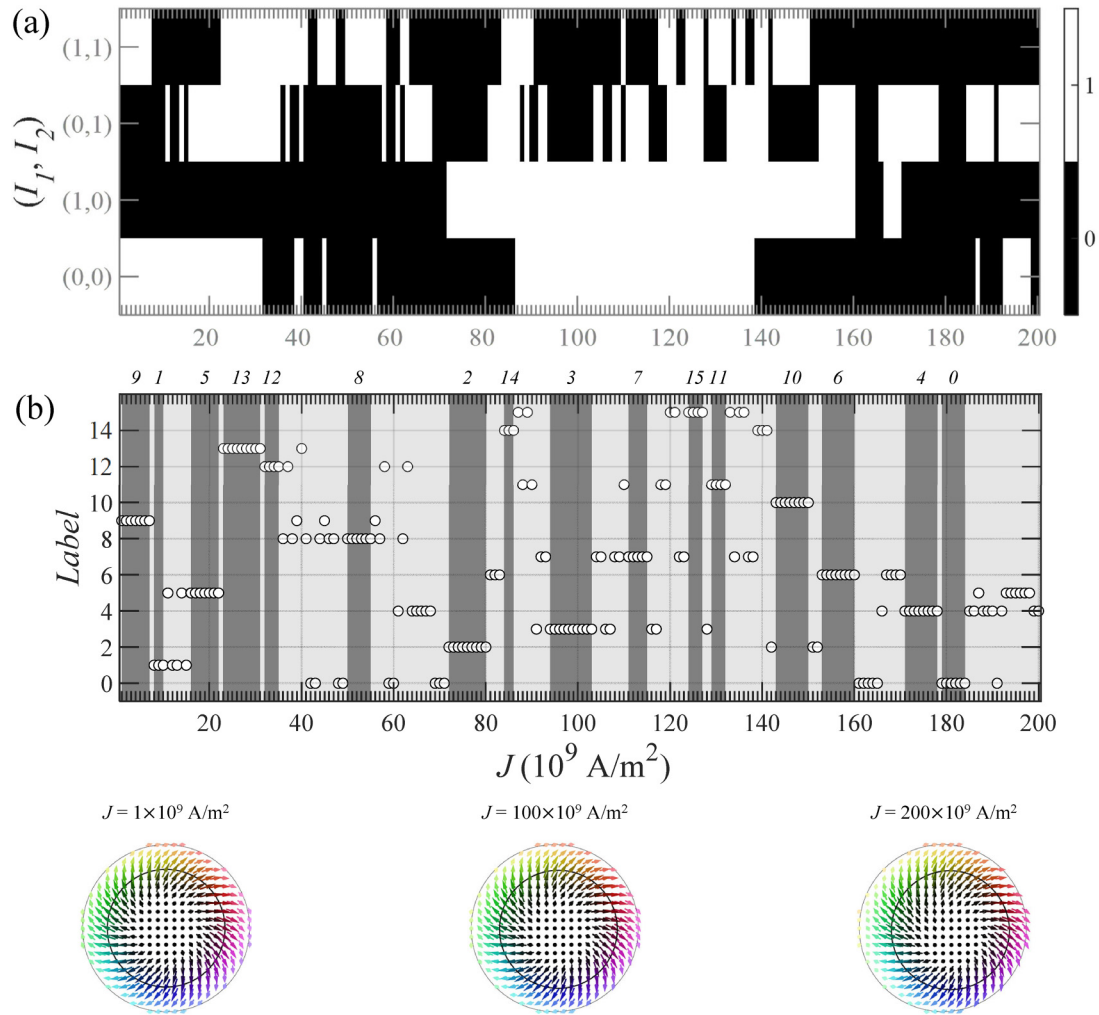


FIG. 5. (a) Outputs for 200 different initial conditions and four different input combinations $(I_1, I_2) = (0, 0), (1, 0), (0, 1),$ and $(1, 1)$, where white represents “true (1),” and black represents “false (0).” The 200 initial conditions were controlled by a current density J ranging from 1×10^9 to 200×10^9 A/m². The four input combinations correspond to four different PMA modulations with κ values of $\frac{282}{800}, \frac{303}{800}, \frac{307}{800},$ and $\frac{572}{800}$, respectively, while f is held constant at 5.5 GHz. (b) Classified logic operations for 200 different initial conditions. White circles represent the resultant logic deduced from (a). Each logic operation is numbered from 0 to 15, as labeled in Table I. Gray regions represent selected initial conditions that cluster into the largest ensemble for each logic as labeled in italic at the top of the figure. The insets show spin configurations for selected initial conditions with specified current densities. In each configuration, a black solid circle denotes the contour plot corresponding to the skyrmion’s radius.

using ensembles of initial conditions. This approach guarantees that initial conditions within the same ensemble lead to consistent outputs.

We prepared 200 different initial conditions for the skyrmion by applying a SOT and skyrmion Hall effect (SkHE) [48] on the skyrmion. For the input combinations of $(I_1, I_2) = (0, 0), (1, 0), (0, 1),$ and $(1, 1)$, we chose four different PMA modulations (f, κ_i, n) , where $i = 1, 2, 3,$ and 4 , respectively. In this study, we set f to 5.5 GHz and n to 10 and examined all possible combinations of κ_i to identify optimal modulation parameters that maximize the clustering of initial conditions and minimize κ_i while ensuring a larger gap between each κ_i . The chosen κ values of $\frac{282}{800}, \frac{303}{800}, \frac{307}{800},$ and $\frac{572}{800}$, correspond to the four input pairs, respectively. For instance, when the input signal is $(1, 0)$, the corresponding PMA modulation applied to the skyrmion, with its designated initial condition, would be $(5.5 \text{ GHz}, \frac{303}{800}, 10)$.

Figure 5(a) illustrates the results from the application of the predefined PMA modulations across 200 distinct initial conditions. A value of Q_{10r} close to 1, indicative of the skyrmion’s core reversal, is set to define the output as “True” (represented in white), while other values are considered “False” (depicted in black). These results demonstrate the sensitivity of Q_{10r} to initial conditions. Notably, the logic gate demonstrates a stronger sensitivity to initial conditions for the modulations of κ_3 and κ_4 [corresponding to input pairs $(0, 1)$ and $(1, 1)$, respectively] compared to κ_1 and κ_2 [corresponding to input pairs $(0, 0)$ and $(1, 0)$, respectively]. Utilizing this data, we can build an initial-condition map for distinct logic operations, displayed in Fig. 5(b). For example, the first initial condition yields outputs of $Q_{10r} = 1, 0, 0,$ and 1 for inputs $(I_1, I_2) = (0, 0), (1, 0), (0, 1),$ and $(1, 1)$, respectively. This logic operation corresponds to the XNOR operation as labeled with “9” in Table I.

Each initial-condition corresponds uniquely to a single logical operation as indicated by white circles. For instance, the first seven initial conditions are associated with the XNOR logic operation. Similarly, the next three initial conditions correspond to the NOR logic operation. However, there are additional initial conditions that correspond to either the XNOR or NOR logic operations. As mentioned, we grouped the largest consecutive initial conditions, sharing the same logic operation, into an ensemble representing the logic operation. There are overall ten initial conditions resulting in the XNOR logic operation (white circles with label “9”). Among them, only the first seven initial conditions are grouped into an ensemble designated for the XNOR operation. Consequently, there are a total of 16 ensembles, each comprising more than three consecutive initial conditions. This approach enhances a device reliability. For example, near $J = 4 \times 10^9$ A/m², the device consistently performs the XNOR logic operation, while around $J = 7 \times 10^9$ A/m², there is a possibility of the NOR operation being performed in real device implementation. These ensembles of initial conditions make the skyrmion in a nanodisk a suitable candidate for reliable chaotic logic gates. We believe that it would be much more energy-efficient to cluster specific logic operations, which are frequently used in real computation (such as six basic logic operations), with initial conditions that can be controlled using lower energies—in this case, current densities. Furthermore, the reliability of the device would significantly increase if each ensemble of initial conditions was made as large as possible. Further details on the characteristics of the initial-condition map, given the parameters (5.5 GHz, κ_i , 10), are available in the Supplemental Material [44]. However, although exploring all combinations of modulation parameters is excessive, variations in (f , n) should also be considered. We propose employing metaheuristic approaches [49] and machine learning techniques for an efficient and accurate construction of the initial-condition map.

IV. DISCUSSION

In this study, we explored the dynamic behaviors of a single skyrmion’s topological charge in circular dots, subjected to sinusoidal PMA modulations with varying parameters. We observed diverse dynamic patterns of the topological charge of the skyrmion exhibiting both ordered and chaotic features, dependent on the specific PMA modulation parameters. Drawing inspiration from the works of Sinha *et al.* [38,39] and leveraging the chaotic conversions of the skyrmion’s topological charge, we proposed a chaotic computation scheme. This scheme features a reconfigurable all-in-one logic device, achievable due to the sensitive dependence on initial conditions of the skyrmion’s chaotic charge conversion, where its’ initial condition can be finely tuned by current densities. The operation and reconfiguration of the logic gates can be rapidly executed within a few nanoseconds through the PMA modulation and current density adjustments, respectively.

To expedite the logic operation time, we can increase the frequency, f , and decrease the number, n , of PMA modulations. Our approach, utilizing the Q state of a single skyrmion confined within a nanodisk, suggests that magnetic materials

with higher damping constants are more preferable, as they allow for quicker overall manipulation time due to faster relaxation time.

A proof-of-concept is feasible using the VCMA approach to apply a vertical voltage across the MTJ, in conjunction with a SOT induced by a parallel current through a heavy-metal layer beneath the MTJ. Field-free magnetization switching in this voltage gated SOT-pMTJ system, comprising IrMn/CoFeB/MgO/CoFeB [50] and W/CoFeB/MgO/CoFeB [51], have been previously reported. Employing these systems, we can also propose a chaotic logic gate that combines SOT-induced chaotic dynamics [52] in the nanodisk with VCMA-controlled initial-condition variations [25], depending on the real device implementation feasibility. The PMA of the nanodisk can be effectively modulated by VCMA up to 10 GHz [53]. Additionally, it is noteworthy that magnetic skyrmion switching via VCMA has been achieved, with a uniform VCMA effect enabling precise control over the skyrmions’ core position through SOT [30]. A sinusoidal VCMA signal can be generated using an external function generator, an RC resonator, or an LC resonator. Implementing appropriate circuit design and shielding can substantially reduce noise susceptibility and promise fault tolerance, thereby preserving the initial condition and chaotic dynamics of the logic gate. Furthermore, alongside our initial-condition ensembles, harnessing a weak chaos [54] could further enhance the device’s reliability.

Compared to the previous chaotic computing paradigms, the current chaotic computation scheme exhibits two distinctions. Firstly, it eliminates the need for setting a separate threshold value for each logic operation. In this scheme, the skyrmion’s switching, rather than surpassing a specific threshold value, is considered as the criterion for “True.” This approach removes the necessity for setting distinct conditions for each logic operation. Secondly, this system operates without a feedback loop, avoiding the need to update chaotic dynamics iteratively. This results in consistent operation times across different logic operations, as each operation is conducted within the same modulation period. These unique characteristics potentially enhance the practical implementation of the proposed chaotic computation scheme in digital computing devices. To extend the scheme’s functionality to unary logic operations, such as the NOT and buffer, which require a single input, we can introduce two additional PMA modulation parameters (κ_5 and κ_6), each corresponding to $I = 0$ and $I = 1$, respectively. This expansion would further benefit the high-density integration of the chaotic logic devices.

The chaotic computation offers reconfigurability, enabling seamless and rapid transitions between various logic operations. This capability significantly lowers integration costs and enhances device density. Moreover, our advanced chaotic computation approach, designed specifically for magnetization manipulation, boosts fault tolerance. This enhancement is achieved by utilizing a set of initial conditions and by evaluating the results based on a uniform criterion: the topological charge conversion of the skyrmions. Our methodology not only facilitates the development of spintronics-based chaotic computing devices but also sheds light on the diverse chaotic behaviors of magnetic skyrmions influenced by changes in

perpendicular magnetic anisotropy. These insights are crucial for advancing skyrmionics technology.

ACKNOWLEDGMENTS

This research was supported by the Basic Science Research Program through the National Research Foundation of Korea (NRF), funded by the Ministry of Science and ICT, South Korea (Grant No. 2021R1A2C2013543) and Samsung Electronics Co., Ltd. (Grant No. IO201229-08274-01). The Institute of Engineering Research at Seoul National University provided additional research facilities for this work.

APPENDIX A: CALCULATION OF THE ENTROPY OF A MARKOV CHAIN

In our analysis, we first identified all unique states within the Q_n sequence to construct a transition matrix. Each element of this matrix initially represented the frequency of transitioning from one state to another, determined by counting consecutive state pairs in the sequence. This matrix was then normalized to convert these frequencies into transition probabilities, which is a critical step in forming our Markov chain model. To calculate the entropy, we employed the Shannon entropy formula [55,56]: $\epsilon = -\sum_i P(i)\log_2 P(i)$. This calculation was performed for each state, and the entropy values were then averaged to derive the mean entropy of the entire Markov chain. This mean entropy value serves as an indicator of the chain's complexity, reflecting the predictability level in the sequence transitions. A higher entropy value implies increased unpredictability and complexity, traits commonly associated with chaotic behavior. This analysis provides deeper insights into the dynamic properties and underlying structure of the Q_n sequence.

APPENDIX B: INITIAL CONDITIONS OF THE SKYRMION

The initial condition of the confined skyrmion can be controlled via its deformation [57], transformation [58], shift, or translation [59]. These changes can be systematically induced using external stimuli such as magnetic fields, electric fields, spin currents, and charge currents. An effective method for manipulating the initial condition of the confined skyrmion involves tracking its guiding center, $\mathbf{R} = (X, Y)$ where $X = \int xq dx dy / \int q dx dy$ and $Y = \int yq dx dy / \int q dx dy$, and $q = (1/4\pi)\mathbf{m} \cdot (\partial_x \mathbf{m} \times \partial_y \mathbf{m})$ is the topological charge density [60].

In our micromagnetic simulation, we assumed a CoFeB/MgO bilayer nanodisk positioned atop a heavy-metal layer, such as Pt [61]. This configuration allows the conversion of a charge current J_c with in-plane direction into a spin current J_s with out-of-plane direction via the spin Hall effect [62]. The spin Hall angle, denoted as α_H , was assumed to have a magnitude of 0.2, and the ratio of the magnitudes of the fieldlike and dampinglike terms, represented as $\xi = \frac{b_l}{a_j}$, was assumed to be -2.0 [63]. The current density, J , was varied in steps of 1×10^9 A/m², ranging from 1×10^9 to 200×10^9 A/m². Due to the SOT, \mathbf{R} moves along the longitudinal direction parallel to the charge current, and due to the SkHE, \mathbf{R} simultaneously moves along the transverse direction. However, this diagonal motion is not a prerequisite for the sensitive dependence on initial conditions. Any variation of the initial magnetic skyrmion, whether linear or nonlinear, is acceptable. We achieved 200 initial states in their equilibrium states. At the beginning of the PMA modulation, we turned off the current. Spin configurations for three different initial conditions, derived from corresponding current densities, are displayed below Fig. 5(b) as insets.

-
- [1] S. Ikeda, K. Miura, H. Yamamoto, K. Mizunuma, H. D. Gan, M. Endo, S. Kanai, J. Hayakawa, F. Matsukura, and H. Ohno, A perpendicular-anisotropy CoFeB–MgO magnetic tunnel junction, *Nat. Mater.* **9**, 721 (2010).
 - [2] S. Mangin, D. Ravelosona, J. A. Katine, M. J. Carey, B. D. Terris, and E. E. Fullerton, Current-induced magnetization reversal in nanopillars with perpendicular anisotropy, *Nat. Mater.* **5**, 210 (2006).
 - [3] H. Meng and J.-P. Wang, Spin transfer in nanomagnetic devices with perpendicular anisotropy, *Appl. Phys. Lett.* **88**, 172506 (2006).
 - [4] B. Dieny and M. Chshiev, Perpendicular magnetic anisotropy at transition metal/oxide interfaces and applications, *Rev. Mod. Phys.* **89**, 025008 (2017).
 - [5] P. V. Ong, N. Kioussis, D. Odkhuu, P. Khalili Amiri, K. L. Wang, and G. P. Carman, Giant voltage modulation of magnetic anisotropy in strained heavy metal/magnet/insulator heterostructures, *Phys. Rev. B* **92**, 020407(R) (2015).
 - [6] Z. Sun, A. Martinez, and F. Wang, Optical modulators with 2D layered materials, *Nat. Photon.* **10**, 227 (2016).
 - [7] R. Y. Umetsu, A. Sakuma, and K. Fukamichi, Magnetic anisotropy energy of antiferromagnetic L1-type equiatomic Mn alloys, *Appl. Phys. Lett.* **89**, 052504 (2006).
 - [8] Q. Yang, T. Nan, Y. Zhang, Z. Zhou, B. Peng, W. Ren, Z.-G. Ye, N. X. Sun, and M. Liu, Voltage control of perpendicular magnetic anisotropy in multiferroic (Co/Pt)₃/PbMg_{1/3}Nb_{2/3}O₃-PbTiO₃ heterostructures, *Phys. Rev. Appl.* **8**, 044006 (2017).
 - [9] D. Wu, Z. Zhang, L. Li, Z. Zhang, H. B. Zhao, J. Wang, B. Ma, and Q. Y. Jin, Perpendicular magnetic anisotropy and magnetization dynamics in oxidized CoFeAl films, *Sci. Rep.* **5**, 12352 (2015).
 - [10] M. Weisheit, S. Fähler, A. Marty, Y. Souche, C. Poinsignon, and D. Givord, Electric field-induced modification of magnetism in thin-film ferromagnets, *Science* **315**, 349 (2007).
 - [11] R.-A. One, H. Béa, S. Mican, M. Joldos, P. B. Veiga, B. Dieny, L. D. Buda-Prejbeanu, and C. Tiusan, Route towards efficient magnetization reversal driven by voltage control of magnetic anisotropy, *Sci. Rep.* **11**, 8801 (2021).
 - [12] A. N. Bogdanov and U. K. Röbner, Chiral symmetry breaking in magnetic thin films and multilayers, *Phys. Rev. Lett.* **87**, 037203 (2001).
 - [13] U. K. Röbner, A. N. Bogdanov, and C. Pfleiderer, Spontaneous skyrmion ground states in magnetic metals, *Nature (London)* **442**, 797 (2006).

- [14] S. Mühlbauer, B. Binz, F. Jonietz, C. Pfleiderer, A. Rosch, A. Neubauer, R. Georgii, and P. Böni, Skyrmion lattice in a chiral magnet, *Science* **323**, 915 (2009).
- [15] H. Vakili, J.-W. Xu, W. Zhou, M. N. Sakib, M. G. Morshed, T. Hartnett, Y. Quessab, K. Litzius, C. T. Ma, S. Ganguly, M. R. Stan, P. V. Balachandran, G. S. D. Beach, S. J. Poon, A. D. Kent, and A. W. Ghosh, Skyrmionics—Computing and memory technologies based on topological excitations in magnets, *J. Appl. Phys.* **130**, 070908 (2021).
- [16] N. Romming, C. Hanneken, M. Menzel, J. E. Bickel, B. Wolter, K. von Bergmann, A. Kubetzka, and R. Wiesendanger, Writing and deleting single magnetic skyrmions, *Science* **341**, 636 (2013).
- [17] S. S. P. Parkin, M. Hayashi, and L. Thomas, Magnetic domain-wall racetrack memory, *Science* **320**, 190 (2008).
- [18] F. Jonietz, S. Mühlbauer, C. Pfleiderer, A. Neubauer, W. Münzer, A. Bauer, T. Adams, R. Georgii, P. Böni, R. A. Duine, K. Everschor, M. Garst, and A. Rosch, Spin transfer torques in MnSi at ultralow current densities, *Science* **330**, 1648 (2010).
- [19] T. Schulz, R. Ritz, A. Bauer, M. Halder, M. Wagner, C. Franz, C. Pfleiderer, K. Everschor, M. Garst, and A. Rosch, Emergent electrodynamics of skyrmions in a chiral magnet, *Nat. Phys.* **8**, 301 (2012).
- [20] S. Woo, K. Litzius, B. Krüger, M.-Y. Im, L. Caretta, K. Richter, M. Mann, A. Krone, R. M. Reeve, M. Weigand, P. Agrawal, I. Lemesh, M.-A. Mawass, P. Fischer, M. Kläui, and G. S. D. Beach, Observation of room-temperature magnetic skyrmions and their current-driven dynamics in ultrathin metallic ferromagnets, *Nat. Mater.* **15**, 501 (2016).
- [21] S. Woo, K. M. Song, H.-S. Han, M.-S. Jung, M.-Y. Im, K.-S. Lee, K. S. Song, P. Fischer, J.-I. Hong, J. W. Choi, B.-C. Min, H. C. Koo, and J. Chang, Spin-orbit torque-driven skyrmion dynamics revealed by time-resolved x-ray microscopy, *Nat. Commun.* **8**, 15573 (2017).
- [22] Z. Wang *et al.*, Thermal generation, manipulation and thermoelectric detection of skyrmions, *Nat. Electron.* **3**, 672 (2020).
- [23] D. Bhattacharya, M. M. Al-Rashid, and J. Atulasimha, Voltage controlled core reversal of fixed magnetic skyrmions without a magnetic field, *Sci. Rep.* **6**, 31272 (2016).
- [24] D. Bhattacharya, S. A. Razavi, H. Wu, B. Dai, K. L. Wang, and J. Atulasimha, Creation and annihilation of non-volatile fixed magnetic skyrmions using voltage control of magnetic anisotropy, *Nat. Electron.* **3**, 539 (2020).
- [25] W. Kang, Y. Huang, C. Zheng, W. Lv, N. Lei, Y. Zhang, X. Zhang, Y. Zhou, and W. Zhao, Voltage controlled magnetic skyrmion motion for racetrack memory, *Sci. Rep.* **6**, 23164 (2016).
- [26] S. Yang, J. W. Son, T.-S. Ju, D. M. Tran, H.-S. Han, S. Park, B. H. Park, K.-W. Moon, and C. Hwang, Magnetic skyrmion transistor gated with voltage-controlled magnetic anisotropy, *Adv. Mater.* **35**, 2208881 (2023).
- [27] K. M. Song, J.-S. Jeong, B. Pan, X. Zhang, J. Xia, S. Cha, T.-E. Park, K. Kim, S. Finizio, J. Raabe, J. Chang, Y. Zhou, W. Zhao, W. Kang, H. Ju, and S. Woo, Skyrmion-based artificial synapses for neuromorphic computing, *Nat. Electron.* **3**, 148 (2020).
- [28] Y. Huang, W. Kang, X. Zhang, Y. Zhou, and W. Zhao, Magnetic skyrmion-based synaptic devices, *Nanotechnology* **28**, 08LT02 (2017).
- [29] T. Yokouchi, S. Sugimoto, B. Rana, S. Seki, N. Ogawa, Y. Shiomi, S. Kasai, and Y. Otani, Pattern recognition with neuromorphic computing using magnetic field-induced dynamics of skyrmions, *Sci. Adv.* **8**, eabq5652, (2022).
- [30] A. H. Lone, X. Zou, G. I. M. Garcia, X. Li, and H. Fariborzi, Spin orbit torque tunable skyrmion neuromorphic devices, in *2022 IEEE International Conference on Emerging Electronics (ICEE)* (IEEE, New York, 2022), pp. 1–5.
- [31] K. Raab, M. A. Brems, G. Beneke, T. Dohi, J. Rothörl, F. Kammerbauer, J. H. Mentink, and M. Kläui, Brownian reservoir computing realized using geometrically confined skyrmion dynamics, *Nat. Commun.* **13**, 6982 (2022).
- [32] D. Pinna, F. Abreu Araujo, J. V. Kim, V. Cros, D. Querlioz, P. Bessiere, J. Droulez, and J. Grollier, Skyrmion gas manipulation for probabilistic computing, *Phys. Rev. Appl.* **9**, 064018 (2018).
- [33] J. Zázvorka, F. Jakobs, D. Heinze, N. Keil, S. Kromin, S. Jaiswal, K. Litzius, G. Jakob, P. Virnau, D. Pinna, K. Everschor-Sitte, L. Rózsa, A. Donges, U. Nowak, and M. Kläui, Thermal skyrmion diffusion used in a reshuffler device, *Nat. Nanotechnology* **14**, 658 (2019).
- [34] C. Psaroudaki and C. Panagopoulos, Skyrmion qubits: A new class of quantum logic elements based on nanoscale magnetization, *Phys. Rev. Lett.* **127**, 067201 (2021).
- [35] C. Psaroudaki, E. Peraticos, and C. Panagopoulos, Skyrmion qubits: Challenges for future quantum computing applications, *Appl. Phys. Lett.* **123**, 260501 (2023).
- [36] G. Park and S.-K. Kim, Emergence of chaos in magnetic-field-driven skyrmions, *Phys. Rev. B* **108**, 174441 (2023).
- [37] L. Shen and K. Shen, Skyrmion-based chaotic oscillator driven by a constant current, *Phys. Rev. B* **109**, 014422 (2024).
- [38] S. Sinha and W. L. Ditto, Dynamics based computation, *Phys. Rev. Lett.* **81**, 2156 (1998).
- [39] S. Sinha and W. L. Ditto, Computing with distributed chaos, *Phys. Rev. E* **60**, 363 (1999).
- [40] J. Torrejon, J. Kim, J. Sinha, S. Mitani, M. Hayashi, M. Yamanouchi, and H. Ohno, Interface control of the magnetic chirality in CoFeB/MgO heterostructures with heavy-metal underlayers, *Nat. Commun.* **5**, 4655 (2014).
- [41] X. S. Wang, H. Y. Yuan, and X. R. Wang, A theory on skyrmion size, *Commun. Phys.* **1**, 31 (2018).
- [42] X. Zhang, Y. Zhou, K. Mee Song, T.-E. Park, J. Xia, M. Ezawa, X. Liu, W. Zhao, G. Zhao, and S. Woo, Skyrmion-electronics: writing, deleting, reading and processing magnetic skyrmions toward spintronic applications, *J. Phys.: Condens. Matter* **32**, 143001 (2020).
- [43] S. Choi, K.-S. Lee, K. Y. Guslienko, and S.-K. Kim, Strong radiation of spin waves by core reversal of a magnetic vortex and their wave behaviors in magnetic nanowire waveguides, *Phys. Rev. Lett.* **98**, 087205 (2007).
- [44] See Supplemental Material at <http://link.aps.org/supplemental/10.1103/PhysRevB.109.174420> for supplementary videos, information about the transition of skyrmions to ferromagnetic states, energetics for different patterns, additional Q_n patterns, the correlation between Q_{10} and Q_{10r} , and the construction of the initial-condition map.
- [45] Y. Guang *et al.*, Electrical detection of magnetic skyrmions in a magnetic tunnel junction, *Adv. Electron. Mater.* **9**, 2200570 (2023).
- [46] I. Lima Fernandes, S. Blügel, and S. Lounis, Spin-orbit enabled all-electrical readout of chiral spin-textures, *Nat. Commun.* **13**, 1576 (2022).

- [47] E. Sirko, Initial conditions to cosmological N -body simulations, or, how to run an ensemble of simulations, *Astrophys. J.* **634**, 728 (2005).
- [48] W. Jiang, X. Zhang, G. Yu, W. Zhang, X. Wang, M. B. Jungfleisch, J. E. Pearson, X. Cheng, O. Heinonen, K. L. Wang, Y. Zhou, A. Hoffmann, and S. G. E. te Velthuis, Direct observation of the skyrmion Hall effect, *Nat. Phys.* **13**, 162 (2017).
- [49] M. Beyki and M. Yaghoobi, Chaotic logic gate: A new approach in set and design by genetic algorithm, *Chaos, Solitons Fractals* **77**, 247 (2015).
- [50] S. Alla, V. Kumar Joshi, and S. Bhat, Field-free switching of VG-SOT-pMTJ device through the interplay of SOT, exchange bias, and VCMA effects, *J. Appl. Phys.* **134**, 013901 (2023).
- [51] Y. C. Wu, K. Garello, W. Kim, M. Gupta, M. Perumkunnil, V. Kateel, S. Couet, R. Carpenter, S. Rao, S. Van Beek, K. K. Vudya Sethu, F. Yasin, D. Crotti, and G. S. Kar, Voltage-gate-assisted spin-orbit-torque magnetic random-access memory for high-density and low-power embedded applications, *Phys. Rev. Appl.* **15**, 064015 (2021).
- [52] L.-M. Kern, K. Litzius, V. Deinhart, M. Schneider, C. Klose, K. Gerlinger, R. Battistelli, D. Engel, C. M. Günther, M.-J. Huang, K. Höflich, F. Büttner, S. Eisebitt, and B. Pfau, Time-resolved imaging reveals transiently chaotic spin-orbit-torque-driven dynamics under controlled conditions, [arXiv:2401.12130](https://arxiv.org/abs/2401.12130).
- [53] R. Matsumoto and H. Imamura, Low-power switching of magnetization using enhanced magnetic anisotropy with application of a short voltage pulse, *Phys. Rev. Appl.* **14**, 021003(R) (2020).
- [54] S. Heiligenthal, T. Dahms, S. Yanchuk, T. Jüngling, V. Flunkert, I. Kanter, E. Schöll, and W. Kinzel, Strong and weak chaos in nonlinear networks with time-delayed couplings, *Phys. Rev. Lett.* **107**, 234102 (2011).
- [55] C. E. Shannon, A mathematical theory of communication, *Bell Syst. Tech. J.* **27**, 379 (1948).
- [56] G. Ciuperca, V. Girardin, and L. Lhote, Computation and estimation of generalized entropy rates for denumerable Markov chains, *IEEE Trans. Inf. Theory* **57**, 4026 (2011).
- [57] Z. Chen, X. Zhang, Y. Zhou, and Q. Shao, Skyrmion dynamics in the presence of deformation, *Phys. Rev. Appl.* **17**, L011002 (2022).
- [58] X. Z. Yu, W. Koshibae, Y. Tokunaga, K. Shibata, Y. Taguchi, N. Nagaosa, and Y. Tokura, Transformation between meron and skyrmion topological spin textures in a chiral magnet, *Nature (London)* **564**, 95 (2018).
- [59] S. Abdizadeh, J. Abouie, and K. Zakeri, Dynamical switching of confined magnetic skyrmions under circular magnetic fields, *Phys. Rev. B* **101**, 024409 (2020).
- [60] N. Papanicolaou and T. N. Tomaras, Dynamics of magnetic vortices, *Nucl. Phys. B* **360**, 425 (1991).
- [61] M. Dai and J.-M. Hu, Field-free spin-orbit torque perpendicular magnetization switching in ultrathin nanostructures, *npj Comput. Mater.* **6**, 78 (2020).
- [62] J. E. Hirsch, Spin Hall Effect, *Phys. Rev. Lett.* **83**, 1834 (1999).
- [63] J. J. Joos, P. Bassirian, P. Gypens, J. Mulkers, K. Litzius, B. Van Waeyenberge, and J. Leliaert, Tutorial: Simulating modern magnetic material systems in mumax3, *J. Appl. Phys.* **134**, 171101 (2023).